INTERNATIONAL JOURNAL OF ADVANCED RESEARCH
International Peer-Reviewed Research Journal
ISSN (Online): 3106-7980 | ISSN (Print): 3106-7972
Volume 3 • Issue 7 • November 2026

SYNTHESIS AND CHARACTERIZATIONS OF Ag DOPPED ZnO NANOSTRUCTURES FOR ELECTROCATALYST AND ADVANCED ELECTRODE MATERIALS FOR ENERGY STORAGE APPLICATIONS

Imad Khan[1], Muhammad Haroon[2], Khalilullah[3], Alamgir Khan[*4], Muhammad Faisal[5], Muhammad Ashfaq[6], Iram Saba[7], Maaz Khan[8], Muneera Altayeb[9]

[1,2] Department of Chemistry, Bacha Khan University Charsadda, KP, Pakistan
[1,2]Department of Chemistry, Government Post Graduate College Charsadda, KP, Pakistan
[3]School of Material Science and Engineering, Beijing Institute of Technology, Beijing 100081, China
*[*4]Department of Physics, Abdul Wali Khan University Mardan, 23200, KP, Pakistan*
[5]National Center of Excellence in Analytical Chemistry University of Sindh Jamshoro Sindh 76080, Pakistan
[6,7]Department of Chemistry, Faculty of Natural Sciences, GC Women University Sialkot-51310, Sialkot, Pakistan
[8]Department of Chemistry, University of Malakand, 18800, Chakdara, Dir Lower, KP, Pakistan
[9]Faculty of Engineering, Hourani Center for Applied Scientific Research, Al-Ahliyya Amman University, Amman, Jordan

[*4]alamgirphy771@gmail.com

DOI: https://doi.org/10.5281/zenodo.24079562

Keywords

Article History
Received: 08 August 2026
Accepted: 22 October 2026
Published: 07 November 2026

Copyright @Author
Corresponding Author: *
Alamgir Khan

Abstract

In this work ZnO, and Ag-dopped ZnO (Ag-ZnO) nanostructures were successfully synthesized via facile hydrothermal method and systematically investigated for photocatalytic, electrocatalytic and energy storage applications. X-ray diffraction (XRD) confirmed the crystalline nature for ZnO and Ag-ZnO with no impurity phases, indicating successful incorporation of Ag in the ZnO. Scanning electron microscopy (SEM) revealed a nanowire morphology for pristine ZnO, while Ag-ZnO exhibited nanowires decorated on nanorods demonstrating significant morphological modification due to Ag doping. Energy disperse X-ray spectroscopy (EDS) verified the elemental composition and confirmed the presence of Zn, O in the ZnO, while Zn, O and Ag in the Ag-ZnO. Photocatalytic degradation studies demonstrated that Ag-ZnO exhibits superior photocatalytic performance compare to pristine ZnO, attributed to enhanced charge separation and improve light absorption. Linear sweep voltammetry (LSV) analysis revealed that 3% Ag-ZnO have over potential of 183 V and Tafel slope of 48 mVdec^{-1} for hydrogen evolution reaction (HER) and overpotential of 180 V and Tafel slope of 52.43 mVdec^{-1} oxygen evolution reaction (OER). Further electrochemical studied show highest specific capacitance of 388.4 F/g at 20 mVs^{-1} for 3% Ag-ZnO from Cyclic voltammetry curve (CV). Electrochemical impedance spectroscopy (EIS) showed lowest charge transfer resistance of 93 Ω, for 3% Ag-ZnO. Galvanostatic charge discharge (GCD) showed highest specific capacitance of 400 F/g at 1 A/g, energy density of 35.55 Wh/kg at 1 A/g and power density of 1688 W/kg at 5 A/g. These results highlight

Ag-ZnO as a promising multifunctional material for electrocatalyst and advanced energy storage applications.

1. Introduction

Water splitting has emerged as a promising and sustainable approach for hydrogen production using renewable energy. [1, 2]. It involves two electrochemical half-reactions, namely the hydrogen evolution reaction (HER) at the cathode and the oxygen evolution reaction (OER) at the anode. However, the practical application of water splitting is limited by the sluggish kinetics of the OER, which involves a complex four-electron transfer process and requires additional energy to overcome the reaction overpotential.[3, 4]. Therefore, developing efficient, cost-effective, and stable electrocatalysts is essential for improving water-splitting performance. Although noble-metal-based catalysts, such as RuO_2 and IrO_2, exhibit excellent OER activity, their high cost and limited availability have encouraged the exploration of alternative metal oxide materials.[5, 6]. Zinc oxide (ZnO) is an attractive metal oxide semiconductor owing to its low cost, natural abundance, chemical stability, and tunable structural properties. Nevertheless, its relatively poor electrical conductivity and limited availability of catalytically active sites can restrict its electrocatalytic performance. To overcome these limitations, elemental doping has been proposed as an effective strategy for modifying the electronic structure, surface properties, and charge-transfer characteristics of ZnO.[7, 8]. In particular, silver (Ag) doping may introduce structural defects, modify the electronic environment, and improve interfacial charge transport, potentially enhancing the accessibility and activity of catalytic sites [9, 10]. Among the possible modification strategies, silver (Ag) incorporation offers an opportunity to tailor the structural, electronic, and surface properties of ZnO. [11, 12]. Depending on the synthesis conditions and silver concentration, Ag may influence crystallite growth, defect formation, surface morphology, and interfacial charge transport. [13, 14]. These changes may improve the accessibility of active sites and modify the adsorption behavior of oxygen evolution intermediates, potentially facilitating the OER. Nevertheless, the effect of Ag depends strongly on its chemical state, distribution, and interaction with the ZnO matrix.[15, 16]. It is therefore important to distinguish genuine lattice doping from the deposition of metallic silver nanoparticles or the formation of separate silver-containing phases. [17, 18]. Previous research on Ag-containing ZnO-based materials has demonstrated promising potential in water-splitting-related applications, although results from photoelectrochemical systems and composite catalysts cannot automatically be generalized to pure electrocatalytic OER systems [19, 20]. Despite these developments, a systematic understanding of the relationship between Ag concentration, structural modification, charge-transfer behavior, and OER performance remains important for designing effective ZnO-based electrocatalysts. Therefore, the present study investigates pristine ZnO and Ag-modified ZnO to evaluate how silver incorporation influences their structural, morphological, and electrochemical properties.[21, 22]. The catalytic performance can be assessed through linear sweep voltammetry (LSV), overpotential, Tafel slope, electrochemical impedance spectroscopy (EIS), and stability measurements. Structural and chemical characterization can further clarify the role of silver in modifying the ZnO matrix [23, 24]. This investigation aims to establish the relationship between material composition and electrochemical behavior and to determine whether controlled Ag incorporation provides a practical strategy for improving the OER performance of ZnO-based materials for sustainable hydrogen production. Furthermore, the increasing demand for efficient energy conversion and storage technologies requires the development of advanced electrode materials with high electrochemical activity, rapid charge-transfer kinetics, and long-term stability [25, 26]. However, the performance of conventional electrode materials is often limited by poor electrical

conductivity, insufficient active sites, and slow interfacial reaction kinetics, which delay their uses in electrocatalytic and energy storage devices [27, 28]. Zinc oxide (ZnO) has attracted significant interest as a potential electrode material due to low cost, chemical stability and tunable nanostructures [29, 30]. As a wider bandgap semiconductor ZnO, exhibits favorable redox behavior and abundant surface-active sites making it suitable for supercapacitor and electrocatalytic applications [31, 32]. The formation of ZnO nanostructures further enhances ion diffusion and surface reactions. Nevertheless, the intrinsic low electrical conductivity and rapid charge carrier recombination of pristine ZnO strictly restrict electron transport and electrochemical efficiency [33, 34]. Incorporation of silver (Ag) into ZnO has emerged as an effective strategy to overcome these limitations. Due to its excellent electrical conductivity and catalytic activity, Ag enhances charge transfer kinetics and reduces interfacial resistance when doped with ZnO [35, 36]. The formation of Ag-ZnO nanostructures promotes efficient charge separation and provided additional electrochemical sites. Consequently, Ag modified ZnO electrodes exhibit enhanced specific capacitance, improve rate capability, reduce overpotential and superior cyclic stability in both electrocatalytic and energy storage [37, 38]. In this work, Ag-ZnO nanostructures were successfully synthesized by hydrothermal method and evaluated for photocatalytic, electrocatalyst and energy storage applications. The incorporation of Ag significantly enhanced the optical and electrical properties of ZnO by improving charge separation and conductivity [39, 40]. AS a result, Ag-ZnO exhibited superior photocatalytic degradation efficiency, enhanced electrocatalyst activity and energy storage performance compare to pristine ZnO. These results indicate that Ag-ZnO is efficient nanostructure for practical applications of electrocatalyst and Advanced electrodes for energy storage devices.

2. Materials and methods

For the synthesis of Ag-ZnO nanostructures zinc nitrate hexahydrate ($Zn(NO_3)_2.6H_2O$ Mw=297.49 g/mol, sigma), sodium hydroxide (NaOH), Mw= 39.997 g/mol, sigma), silver nitrate ($AgNO_3$), Mw=169.87 g/mol, sigma) DI, water and ethanol is used starting materials.

2.1 Synthesis of Pure ZnO

Pure ZnO nanowires are synthesized by hydrothermal method. In typically synthesis 2.97 g, of zinc nitrate hexahydrate ($Zn(NO_3)_2.6H_2O$ was dissolved in 50 ml of deionized water under continuous magnetic stirring to obtain a clear solution. Separately, 0.8 g of sodium hydroxide (NaOH) was dissolved in 50 ml of deionized water, and the resulting solution was added dropwise to the zinc nitrate solution while stirring until the PH value of the mixture reached to approximately (10-11). The homogenous solution then transfers to 150 ml, Teflon line stainless steel autoclave and heated at 160 °C, for 12 hours. After completion of the reaction the autoclave was allowed to cool naturally to room temperature. The resulting white precipitate was collected by centrifugation and washed several times with deionized water and ethanol. Finally, the product was dried at 80 °C for 10 hours and calcined at 400 °C for 2 hours to obtained the ZnO nanowires.

2.2 Synthesis of Ag dopped ZnO (Ag-ZnO)

For the 1% Ag-ZnO sample 2.94 g of zinc nitrate hexahydrate ($Zn(NO_3)_2.6H_2O$ and 0.017 g of silver nitrate ($AgNO_3$) were dissolved in 50 ml, DI water under continuous magnetic stirring. For the 3% Ag-ZnO 2.88 g, of ($Zn(NO_3)_2.6H_2O$ and 0.051 g of $AgNO_3$, and for 5% Ag-ZnO 2.83 g of ($Zn(NO_3)_2.6H_2O$ and 0.85 g of $AgNO_3$ were used. In each case 0.8 g, of NaOH, was dissolved in 50 ml, of deionized water and added dropwise to the metal precursor solution until the PH value reaches to (~10-11). The homogenous solution then transfers to 150 ml, Teflon line stainless steel autoclave and heated at 160 °C, for 12 hours. After completion of the reaction the autoclave was allowed to cool naturally to room temperature. The resulting white precipitate was collected by

centrifugation and washed several times with deionized water and ethanol. Finally, the product was dried at 80 °C for 10 hours and calcined at 400 °C for 2 hours to obtained the Ag-ZnO nanostructures.

2.3 Characterizations

The x-ray diffractometer (JDX-3532, Japan), Scanning electron microscopy (SEM) (JSM-IT-1OO), and energy dispersing x-ray spectrometer (EDS) (JEOL JSM-IT-100) were used to evaluate the phase, surface morphology, and elemental composition of the produced samples. For electrochemical properties Gamry interface series are used.

1.1 Fabrication of Supercapacitor and electrochemical measurement

On a nickel (Ni) foam substrate, the electrodes needed to evaluate the electrochemical performance were created using a simple brushing technique. The anode material included eighty weight percent produced Ag-ZnO nanostructure, ten weight percent activated carbon (AC), and ten weight percent polyvinylidene fluoride (PVDF) as a binder. The cathode material comprised 90 percent by weight activated carbon and 10 weight percent PVDF. The two electrodes were divided by filter paper, forming the asymmetrical supercapacitor configuration. Two electrodes were employed to evaluate the electrochemical performance of the fabricated supercapacitor. A Gamry Interface 1000E potentiostat was employed for measurements, encompassing galvanostatic charge-discharge (GCD), electrochemical impedance spectroscopy (EIS), and cyclic voltammetry (CV). The asymmetric supercapacitor charges and discharges at a current density of (1-5) A/g within a potential window of 0 to 0.8 V, and the CV test scan speeds vary from 20 to 100 mVs^{-1}. The specific capacitance was calculated using Eq. (2) [43, 44] using cyclic voltammetry analysis.

$$Cs = \frac{\int I \times \Delta V}{\kappa m_a \Delta V} \quad (2)$$

Where $\int I \times \Delta V$ denote area under CV, curve m_a represents mass of the active material, K represent scan rate and ΔV represent the potential window of the prepared electrodes. Equations (3) [45], (4) [46], and (5) [47],were used to compute the specific capacitance, energy density, and power density from the GCD curves.

$$Cs = \frac{I \times \Delta V}{m_a \times \Delta t} \quad (3)$$

$$E = \frac{1}{2}\left(\frac{Cs \times \Delta V^2}{3.6}\right) \quad (4)$$

$$P = \frac{3600 \times E}{\Delta t} \quad (5)$$

Here, I denote the current applied, while Δt signifies the discharging duration.

2. Results and discussion

2.1 X-ray diffraction (XRD)

The x-ray diffraction (XRD) of the prepared ZnO, 1% Ag-ZnO, 3% Ag-ZnO and 5% Ag-ZnO nanostructures is show in Fig.1. The diffraction angle 2θ is varying between 20 to 80 degrees. All the observed peaks are will match with the standard XRD JCPD card number (043-0002) for Wurtzite structure of ZnO, and (04-0783) for face centric cubic structure of Ag. The XRD, structure of Ag-ZnO shows the successful incorporation of Ag into the ZnO and there are no extra peaks observed which shows the purity of as prepared materials. The crystallite sizes are calculated by Scherer's Eq. (6) for ZnO, 1% Ag-ZnO, 3% Ag-ZnO and 5% Ag-ZnO are 37 nm, 27 nm and 22 and 24 nm respectively. The progressive reduction in crystalize size upon Ag doping indicates that Ag incorporation effectively defeats ZnO crystal growth [48, 49]. This behavior is attributed to lattice distortion and increased macrostrain caused by the substitution of larger Ag^+ ions (1.26 Å) for Zn^{2+} ions (0.74 Å) or their career of interstitial sites, which delays atomic diffusion to crystal growth [50, 51]. The minimum crystallite size observed at 3% Ag-ZnO, suggests an optimal dopant concentration for growth inhibition. The slight decrease at 5 % Ag-ZnO, may be due to dopant agglomeration, partial strain relaxation, or the formation of Ag rich-clusters, enabling grain

growth [52]. The non-monoatomic trend reflects the competition between lattice distortion and dopant segregation effects.

$$D = \frac{k\lambda}{\beta cos\theta} \quad (6)$$

D, represents the crystalize size, K represents the shape factor, λ represent wavelength of x-ray where B, represents full width and θ represents the angle.

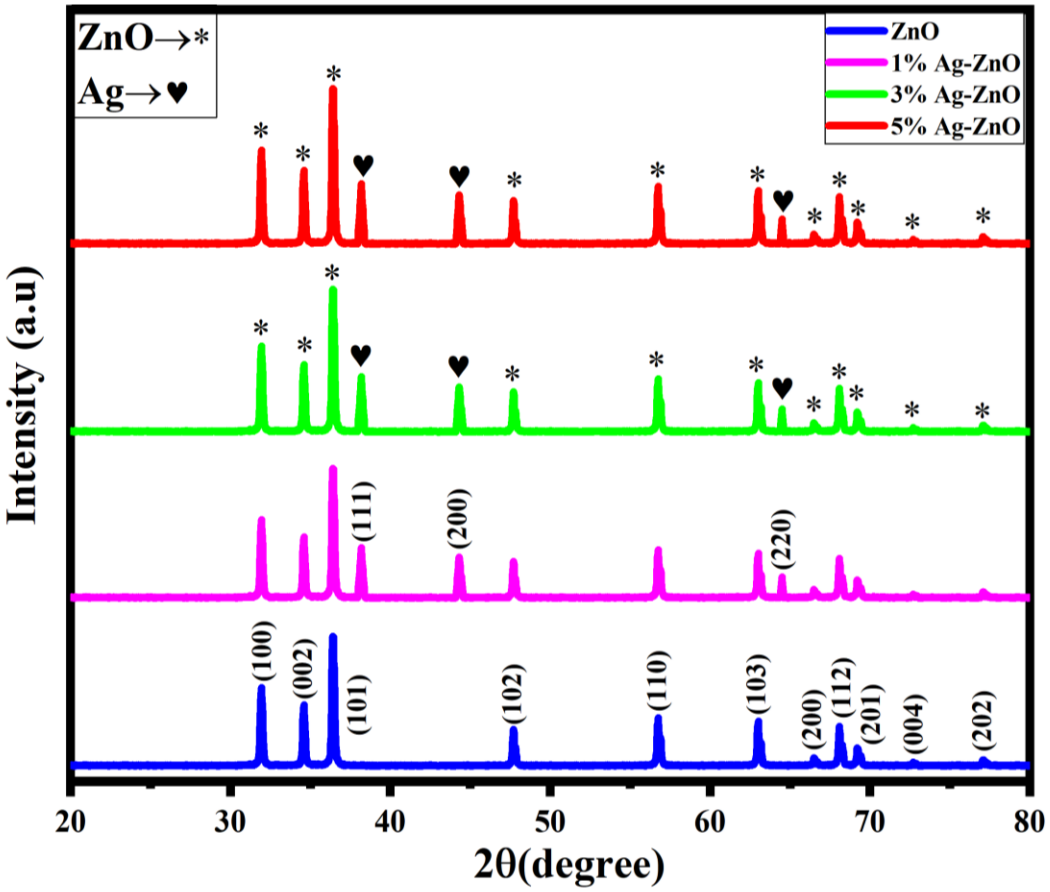


Fig.1: XRD, pattern of ZnO, 1% Ag-ZnO, 3% Ag-ZnO and 5% Ag-ZnO respectively.

2.2 SEM, EDS analysis

Fig.2 (a-d) shows the low magnification and the insect show high magnification SEM, images for pure ZnO, 1% Ag-ZnO, 3% Ag-ZnO and 5% Ag-ZnO respectively. SEM, morphology reveals that pure ZnO have nanowires like structure with smooth surfaces and well-defined hexagonal geometry indicating anisotropic growth along c-axis of the wurtzite structure [53, 54]. When the Ag incorporation in the ZnO, 1% Ag-ZnO, 3% Ag-ZnO and 5% Ag-ZnO a distinct morphology is observed where ZnO nanowires decorated on the surface of thicker nanorods forming hierarchical nanowires-nanorods like morphology. This decoration becomes more pronounced with increasing Ag content, suggesting that Ag incorporation modifies the nucleation density and growth kinetics [55]. Fig.2 (e-h) shows the energy disperse x-ray spectroscopy (EDS) of ZnO, 1% Ag-ZnO, 3% Ag-ZnO and 5% Ag-ZnO. The undoped sample show Zn and O peaks indicating high purity of the ZnO. For Ag-ZnO samples additional peaks of Ag are observed in the 1% Ag-ZnO, 3% Ag-ZnO and 5% Ag-ZnO indicate the successful

incorporation of Ag into the ZnO. The intensity of Ag is increasing when the dopant concentration is increases in the ZnO, demonstrating effective control over Ag content [56, 57].

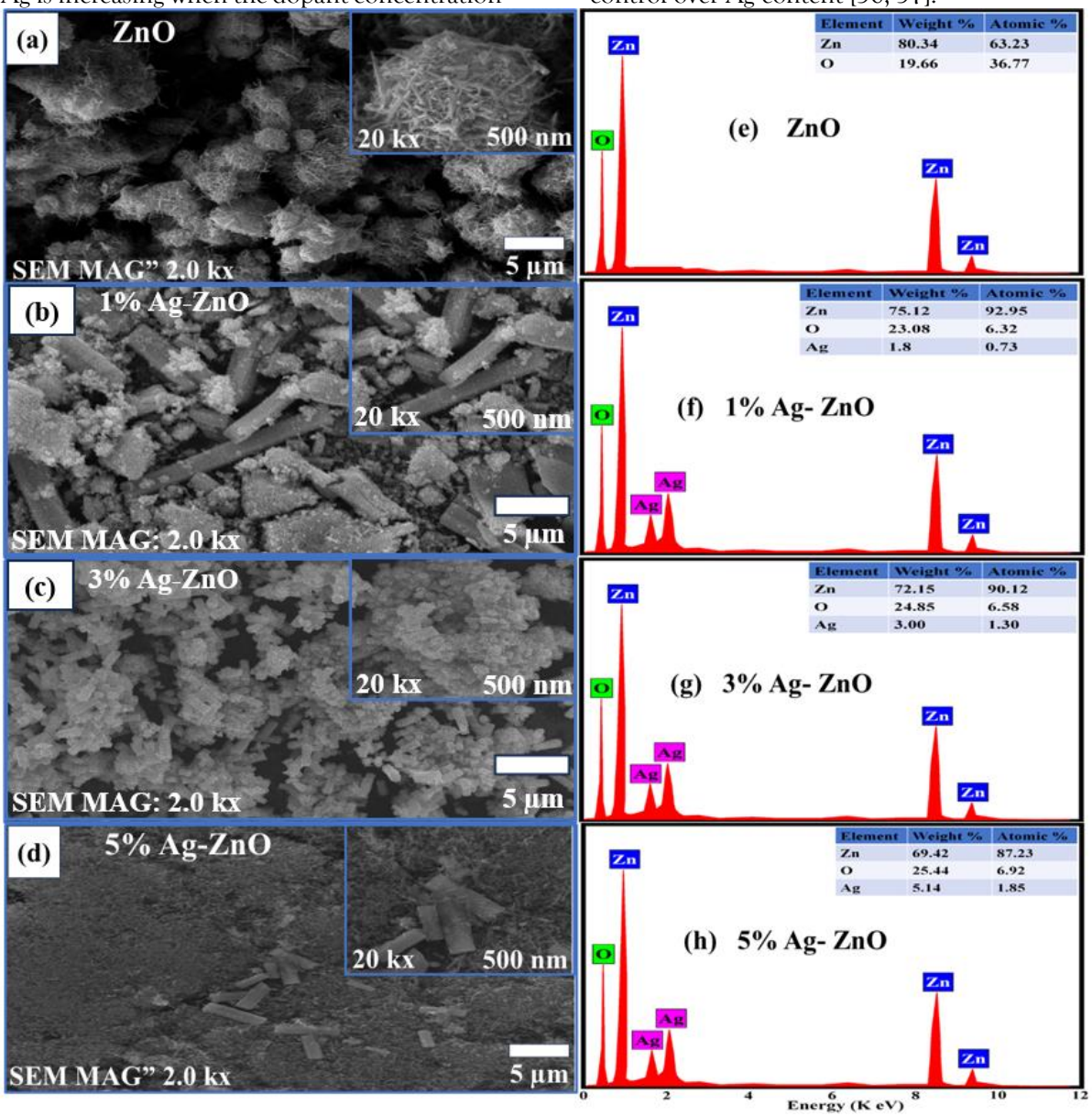


Fig.2 (a-d) SEM while (e-h) EDS spectrum for ZnO, 1% Ag-ZnO, 3% Ag-ZnO and 5% Ag-ZnO respectively.

1.1 Linear sweep voltammetry (LSV)

To investigate the electrocatalysts properties of prepared electrodes linear sweep voltammetry analysis was performed in KOH (3M) solution at 20 mV/s. The LSV polarization curves can be seen in Fig.5 (a) for oxygen evolution reaction (OER). The pristine ZnO electrode exhibits low electrocatalytic activity for OER, characterized by a weak current response and high overpotential (~390 mV) indicating slow kinetics [58]. Upon Ag doping a pronounced enhancement in catalytic performance is observed. The 1% Ag-ZnO sample shows a noticeable increase in peak current density and a reduce in overpotential (~290 mV) suggesting improved charge transfer and active site availability. Further improvement is achieved for

3% Ag-ZnO which displays the highest peak current and lowest overpotential (~180 mV), reflecting optimal Ag dispersion and synergistic interaction between Ag and ZnO is seen in Fig.5 (b). However, at higher doping 5% Ag-ZnO, the catalytic activity declines with an increased overpotential (~240 mV) likely due to Ag agglomeration and partial blockage of active sites [59, 60]. The Tafel slope values follow a similar trend decreasing from 93.42 $mVdec^{-1}$ for ZnO to 74.56 $mVdec^{-1}$ for 1% Ag-ZnO and reaching a minimum 52.43 $mVdec^{-1}$ for 3% Ag-ZnO Fig.5 (c), indicating accelerated reaction kinetics [61]. The increases in Tafel slope to 63.32 $mVdec^{-1}$ for 5% Ag-ZnO further confirms the fall in catalytic efficiency at higher Ag content. The hydrogen evolution reaction (HER) performance of as prepared electrodes is display in Fig.5 (d). Pristine ZnO, shows a high overpotential (~367 mV), Fig.5 (e), and a Tafel slope of 113 $mVdec^{-1}$ Fig.5 (f), reflecting its limited electrical conductivity and weak hydrogen absorption capability [62]. The 1% Ag-ZnO electrode exhibited a reduced overpotential (~256 mV) and a Tafel slope 85 $mVdec^{-1}$ indicating improved electron transport across the electrode-electrolyte interface [63]. The 3% Ag-ZnO catalyst achieved the most favorable HER kinetics, with an overpotential (~183 mV) and a Tafel slope of 48 $mVdec^{-1}$ suggesting an optimized balance between active site density and charge transfer efficiency. In contrast, the 5% Ag-ZnO electrode showed a moderate increase in overpotential (~220 mV), and Tafel slope 64 $mVdec^{-1}$ which may be associated with excessive metallic coverage that alters the surface reaction pathway and reduces the accessibility of catalytically favorable sites [64]. The calculated overpotentials and Tafel slope values are display in table 2. These results confirm that controlled Ag doping effectively modulates the electrocatalyst properties of ZnO leading to enhanced (OER and HER) kinetics at an optimal doping level [65].

Table 2: Current density, over potential and Tafel slope values of as prepared electrodes.

Electrode	Scan rate (mVs^{-1})	Current density ($mVcm^{-2}$)	Over potential (mV) OER	Over potential (mV) HER	Tafel slope OER ($mVdec^{-1)}$	Tafel slope HER ($mVdec^{-1}$)
ZnO	20	10	390	367	93.42	113
1% Ag-ZnO	20	10	290	256	74.56	85
3% Ag-ZnO	20	10	180	183	52.43	48
5% Ag-ZnO	20	10	240	220	63.32	64

INTERNATIONAL JOURNAL OF ADVANCED RESEARCH
International Peer-Reviewed Research Journal
ISSN (Online): 3106-7980 | ISSN (Print): 3106-7972
Volume 3 • Issue 7 • November 2026

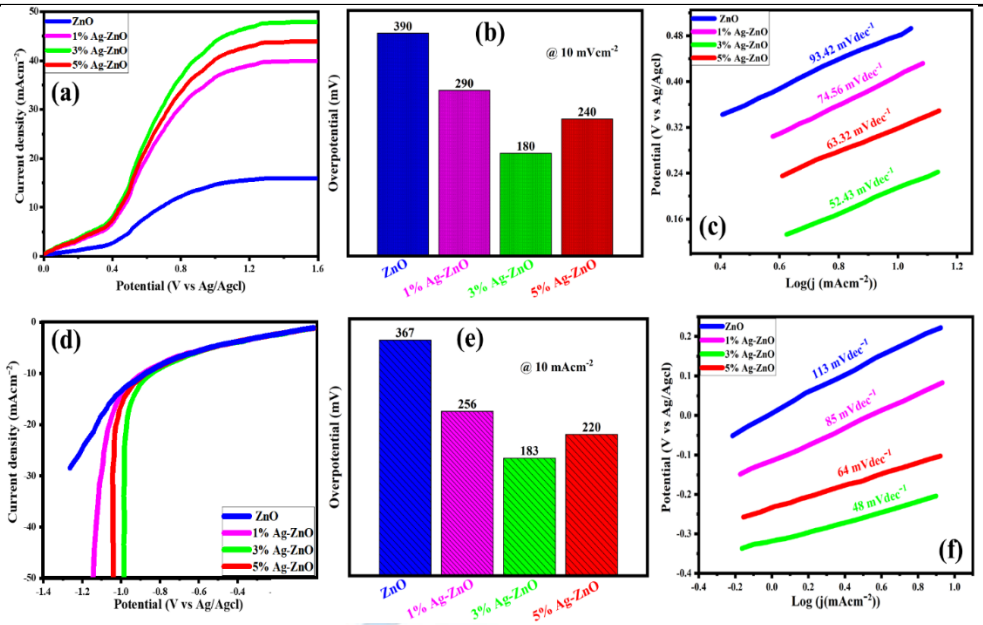


Fig.5: LSV curves of (a) OER, (b) Overpotentials for OER, (c) Tafel slope for OER, while (d) LSV curves for HER, (e) overpotentials for HER, and (f) Tafel slope for HER for ZnO, 1% Ag-ZnO, 3% Ag-ZnO and 5% Ag-ZnO respectively.

1.2 Electrochemical asymmetric supercapacitor response

Cyclic voltammetry (CV), Electrochemical impedance spectroscopy (EIS), and Galvanostatic static charge discharge (GCD) were among the characterization techniques used to assess the super capacitor's electrochemical performance. The supercapacitor arrangement uses activated carbon as the cathode and ZnO, 1% Ag-ZnO, 3% Ag-ZnO and 5% Ag-ZnO nanostructures as the anode. To guarantee enough isolation, a separator was positioned in between the electrodes. To assemble the aqueous supercapacitor device, many drops of 3M KOH electrolyte were put to the filter paper prior to testing. Fig.6 (a-d) displays the CV curves for ZnO, 1% Ag-ZnO, 3% Ag-ZnO and 5% Ag-ZnO nanostructure-based electrodes at various scan rates (20 to 100 mVs^{-1}). Even at higher scan rates, all electrodes showed two clear and distinct redox peaks that matched the anode materials' battery-type behavior. The Ag-ZnO, nanostructure-based electrode curves show how an intrinsic electric field forms at the Ag doped ZnO pn-junction interface [66, 67]. As further evidenced by the capacitance vs scan rate plot in Fig.6 (f), this built-in field efficiently reduces polarization effects by encouraging a more uniform charge distribution, hence enhancing capacitance stability with different scan rates. The findings support the successful creation of a distinct pn-junction between nickel and ZnO, which is ascribed to the metal precursors' heat treatment after using the hydrothermal synthesis method [68]. This procedure helps to eliminate any remaining organic species and improves the transition metal oxide's crystallinity. Moreover, it promotes interdiffusion and interfacial reaction between the metal oxide which strengthen the adhesion and electronic coupling at the pn-junction interface ultimately contributing to superior electrochemical performance [69, 70]. Additionally, it is evident that there is a relationship between the rise in scan rate and the fall in Specific capacitances (Cs). The ion exchange mechanism that takes place at the electrode surface explains, at reduced scan rate values, OH ions possess sufficient time to diffuse into the electrode materials [71]. Conversely, at high scan rates, the extent of ion accessibility within the electrode materials decreases. The Dunn method

is utilized to confirm that ion diffusion is blocked. ZnO, 1% Ag-ZnO, 3% Ag-ZnO and 5% Ag-ZnO exhibited specific capacitances of 75.72, 260.13, 388.4, and 161.2 F/g respectively. As demonstrated by the maximum specific capacitance seen for the 3% Ag-ZnO electrode in comparison to the ZnO, 1% Ag-ZnO and 5% Ag-ZnO electrodes, the ZnO nanowires on the Ag nanorods have enhanced the diffusion of ions from the electrolyte to the electrode surface by increasing the electrode's surface area, which raises the surface energy [72]. The increase of surface area enhances specific capacitance by offering additional active sites for electrochemical reactions. Furthermore, as shown in Fig.6 (f), the incorporation of Ag doping into the ZnO creates a more interconnected and porous structure that facilitates effective ion diffusion inside the electrode material [73, 74]. Thus, the overall outstanding performance of the suggested 3% Ag-ZnO based ASCs electrode is assumed to be due in part to improved ion diffusion. The specific capacitance for 5% Ag-ZnO electrode decreases it is due to reduce surface area as Ag doping increasing which can block pores and aggregate reducing electroactive surface area and increased charge transfer resistance where excess Ag creates defects delay electron transfer and disrupted ZnO structure were lattice distortion effects ion diffusion and charge storage [75, 76].

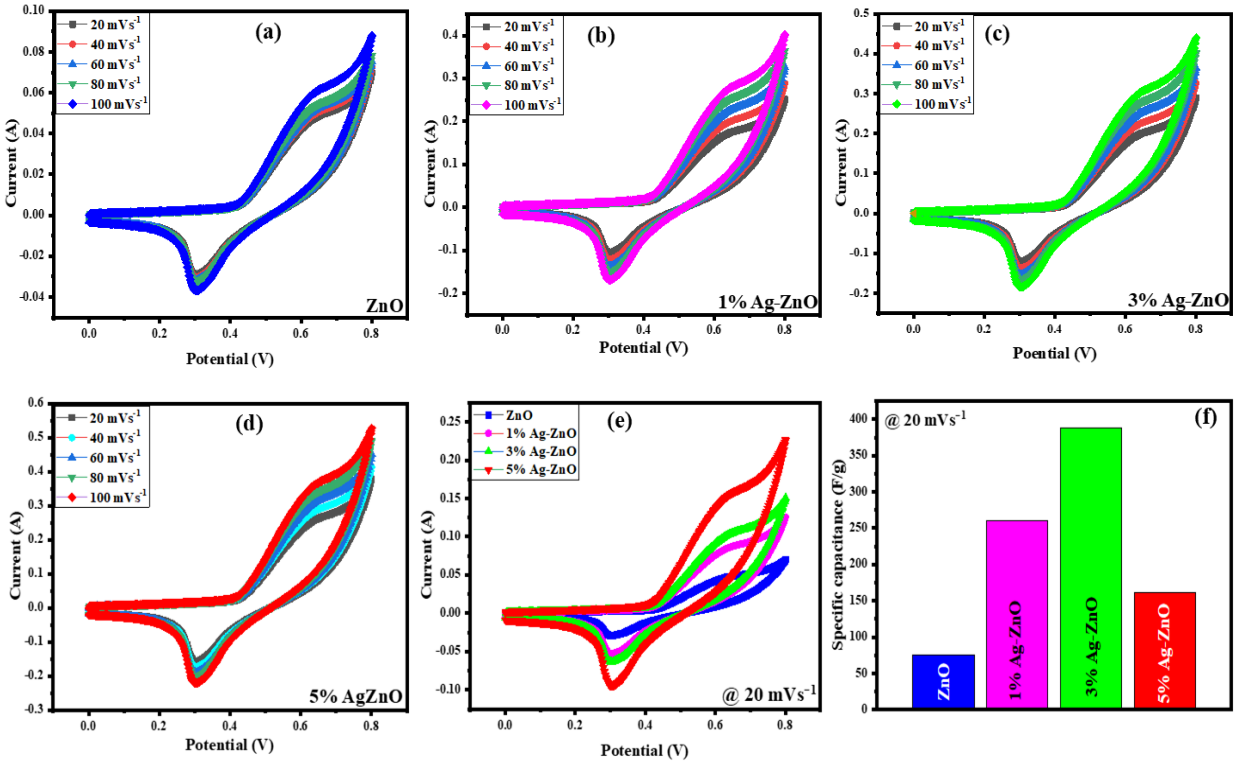


Fig.7 CV curves of (a) ZnO, (b) 1% Ag-ZnO, (C) 3% Ag-ZnO and (d) 5% Ag-ZnO, (e) comparatively CV of as prepared electrodes at 20 mVs^{-1} (f) specific capacitances vs scan rate of as prepared electrodes.

A thorough examination of the CV curves at various scan rate values was carried out in order to gain a better understanding of the kinetics of an electrochemical reaction involving the ZnO, 1% Ag-ZnO, 3% Ag-ZnO and 5% Ag-ZnO nanostructure-based electrodes. Peak current (I) and scan rate (κ) were shown in Fig.8 (a-d) to be related using the power-law Eq. (10) [77],

$$\log(i) = b\log(\kappa) + \log(a) \quad (10)$$

INTERNATIONAL JOURNAL OF ADVANCED RESEARCH
International Peer-Reviewed Research Journal
ISSN (Online): 3106-7980 | ISSN (Print): 3106-7972
Volume 3 • Issue 7 • November 2026

Where the charging and discharging processes are influenced by the empirical constants a, and b. The charging and discharging processes of the capacitor electrode are typically caused by the diffusion-limited reaction when b is near unity, On the other hand, diffusion largely governs the charging and discharging processes if b is around 0.5 [70, 79]. According to Fig.11 (h), the corresponding

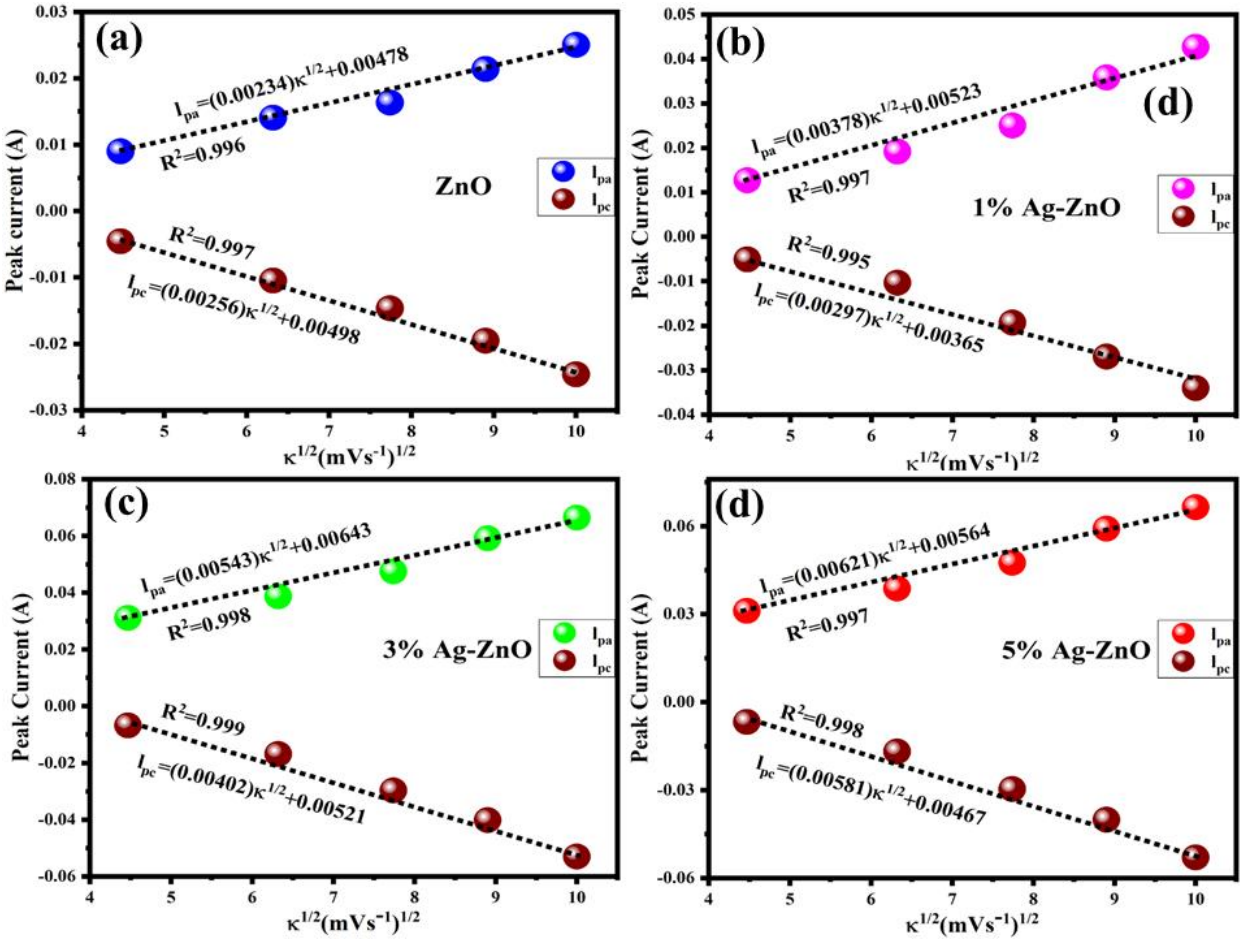


Fig.8: peak current vs scan rate (a) ZnO, (b) 1% Ag-ZnO, (c) 3% Ag-ZnO and (d) 5% Ag-ZnO respectively.

b values for ZnO, 1% Ag-ZnO, 3% Ag-ZnO and 5% Ag-ZnO electrodes are 0.43, 0.64, 0.51, and 0.56 respectively. This indicates that diffusion control reactions dominate the produced charge storage kinetics. The Dunn approach was applied using the following Eq. (11) [80],in order to precisely ascertain the percentage of capacitive and diffusion contributions that comprise the total specific capacitance.

$$\frac{i(V)}{\kappa^{1/2}} = \gamma_1 \kappa^{1/2} + \gamma_2 \quad (11)$$

Where κ is the scan rate, γ_1 is the slope, γ_2 is the y-intercept derived from the linear fit, and I (V) is the peak current response. In this case, the capacitive current contribution is represented by $i_c = \gamma_1 \kappa$, and the diffusion current contribution is represented by $i_d = \gamma_2 \kappa^{1/2}$. The combination of capacitive (i_c) and diffusion (i_d) contributions for ZnO, 1% Ag-ZnO, 3% Ag-ZnO and 5% Ag-ZnO electrodes are displayed at different scan rates in Fig.9 (a-d), respectively. Given the short time allotted for ion diffusion, it is clear that the capacitive contribution predominates with a

greater scan rate [81, 82]. Moreover, low scan rate values are where the diffusion-controlled charge storage is most noticeable. The contribution rates of ZnO, and 1% Ag-ZnO, electrodes are comparable and nearly identical. In contrast, 3% Ag-ZnO electrode exhibits a roughly 50% contribution from capacitive current and a roughly 50% contribution from diffusion current. Effective ion diffusion between ZnO and the KOH within the electrode can be promoted by the presence of Ag which can offer a more porous and linked channel. For 5% Ag-ZnO again this value are decreases to 40% and 60%. To gain a deeper comprehension, the capacitance contributions from the inner and outer surfaces of the electrode materials were identified and distinguished using Trasatti's approach based on the following Cottrell's Eq. (12) [83] ,

$$i(\kappa) = (2.69 \times 10^5) n^{3/2} A D_0^{1/2} C_o^* \kappa^{1/2} \quad (12)$$

The charges carried on the electrode surface, electrode area, and concentration are denoted by n, A, and C_o^* , respectively, while the diffusion coefficient is denoted by Do. The total current at a particular scan rate is shown. This approach is based on the kinetic theories of surface charge and diffusion-controlled charge, which react differently to an increase in the applied potential scan rate. Under the assumption of semi-infinite diffusion, the following Eq. (13) [84], illustrates how these mechanisms have distinct effects on the overall charge contribution, which can be comprehended by deconvoluting these two contributions.

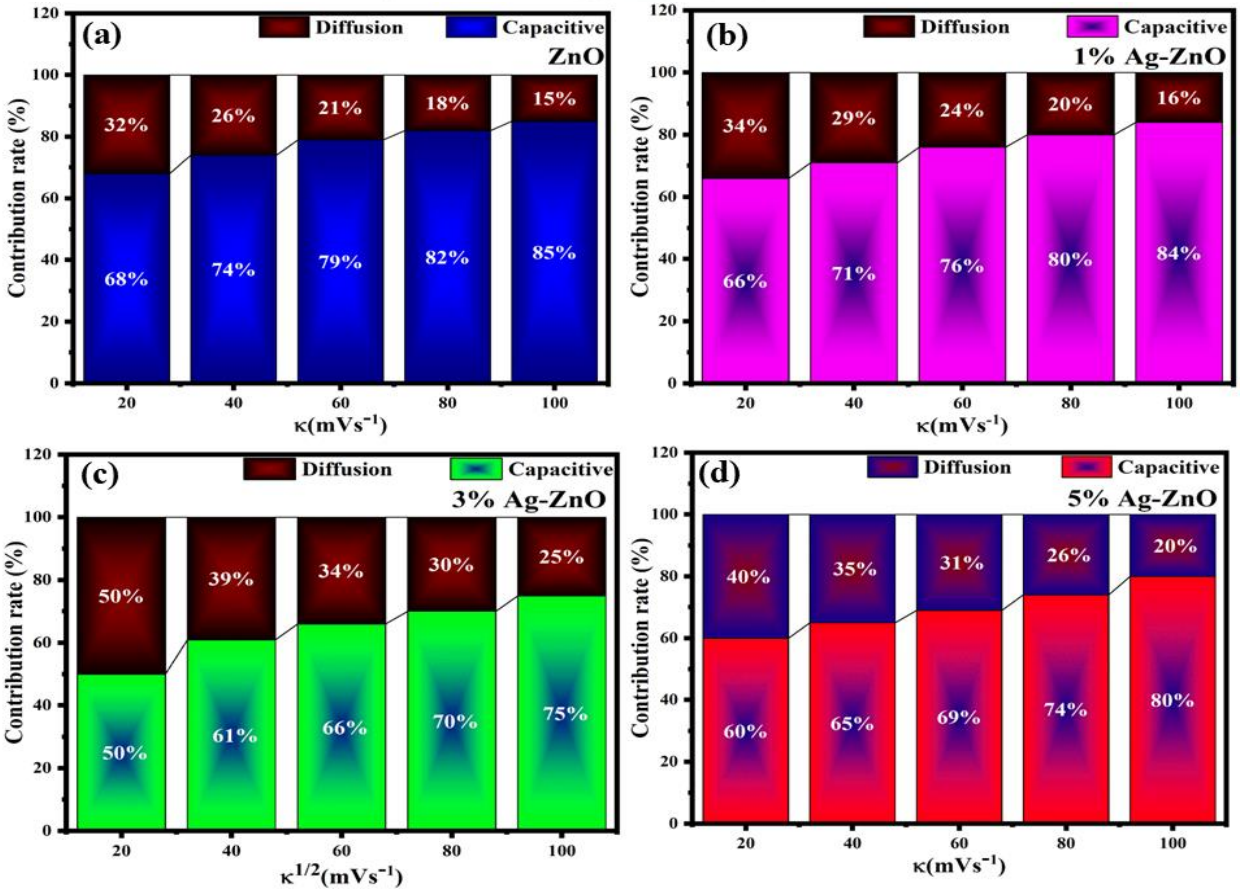


Fig.9: Contribution rate vs scan rate (a) ZnO, (b) 1% Ag-ZnO, (c) 3% Ag-ZnO and (d) 5% Ag-ZnO respectively.

INTERNATIONAL JOURNAL OF ADVANCED RESEARCH
International Peer-Reviewed Research Journal
ISSN (Online): 3106-7980 | ISSN (Print): 3106-7972
Volume 3 • Issue 7 • November 2026

$$q_T = q_i + q_o \Rightarrow C_T = C_i + C_o \quad (13)$$

When κ→+∞, q→qo was employed, the capacitive contribution from the outer surface was calculated using Eq. (14) [85], since it is the more accessible portion of the electrode during the electrochemical reaction. A linear correlation is obtained by plotting the computed 1/Cs against κ1/2, as Fig.10 (e) illustrates. The surface contribution is obtained by linearly fitting the graphic and then extrapolating the fitted line to the y-axis.

$$C(\kappa) = \frac{constant}{\sqrt{\kappa}} + C_o \quad (14)$$

With boundary conditions κ→0, q→q_T, the following Eq. (15) [86], was used for the inner surface because such contributions needed enough time for electro active species to disperse. The total capacitance (CT), which is determined by adding the capacitances from the inner and outer surfaces, is the reciprocal of the y-intercept of the 1/Cs vs. $\kappa^{1/2}$ plot, as shown in Fig.10 (f).

$$\frac{1}{C(\kappa)} = constant\ \sqrt{\kappa} + \frac{1}{C_T} \quad (15)$$

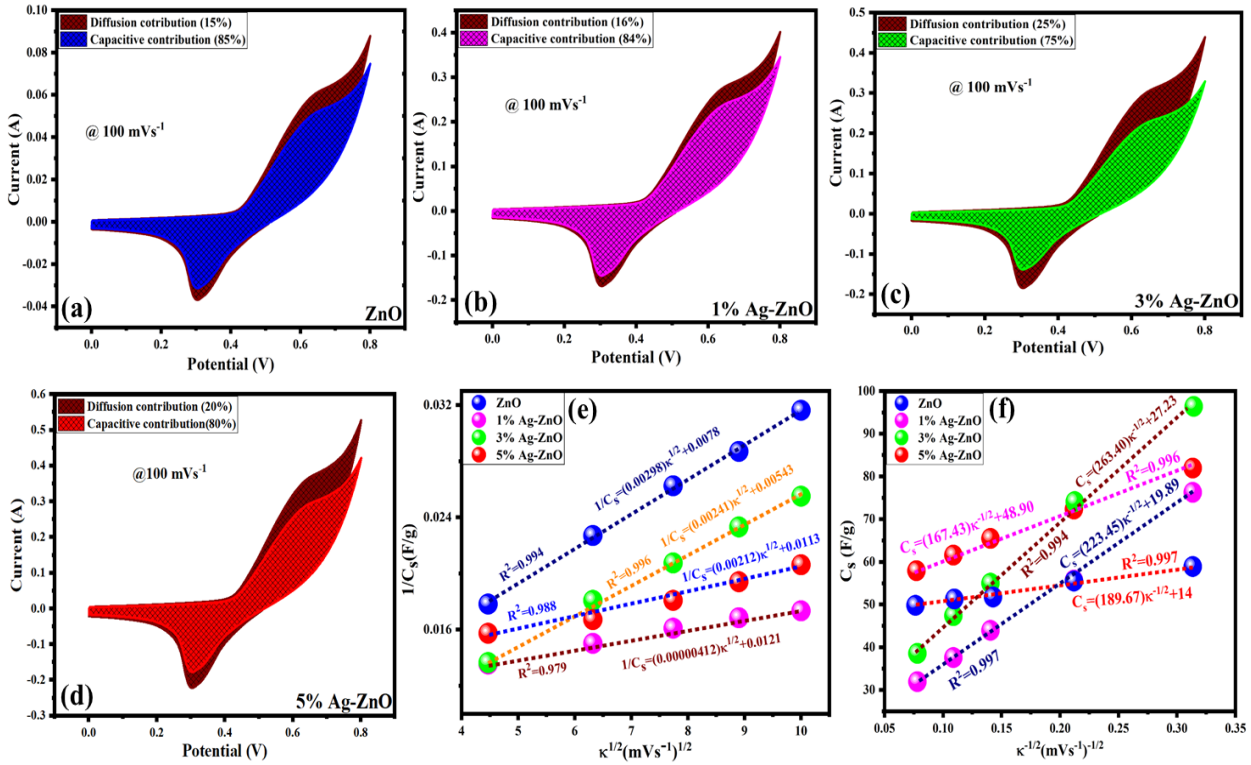


Fig.10: Inner and outer surface contribution of (a-d) while (e) 1/C_s vs $K^{1/2}$ (f) C_s vs $K^{-1/2}$ for ZnO, 1% Ag-ZnO, 3% Ag-ZnO and 5% Ag-ZnO respectively.

Fig.10 (e) shows the ZnO and Ag contributions from the 5% Ag-ZnO nanostructure's inner surface. It was found that the inner surface contributions of Ag and ZnO were approximately 56.43 and 43.57 percent, respectively. The surface contributions of 3% Ag-ZnO exhibited considerable variation, with the Ag contribution comprising 3.21% of the total contribution. This rise in the interior contribution to about 96.79% indicates that Ag growth opens up additional

channels for electrochemical reactions during redox events and that Ag and ZnO cling to one another well, which makes it easier for OH ions to move [87]. These results are in line with the Rendle Sevicks (b) values, which are displayed in Fig.11 (h) and show a drop in b values from approximately 0.56 to approximately 0.51 as the diffusion current control reaction approaches [88]. Fig.11 (g) displays the electrochemical impedance spectroscopy (EIS) of the prepared electrodes. The charge transfer resistance of ZnO, 1% Ag-ZnO, 3% Ag-ZnO and 5% Ag-ZnO are 220, 115, 90.5 and 150 Ω, respectively. The 3% Ag-ZnO electrode show lowest charge transfer resistance is compare to pure ZnO, 1% Ag-ZnO and 5% Ag-ZnO electrodes. Fig.11 (a-d) shows galvanostatic charge-discharge (GCD) curves of the ZnO, 1% Ag-ZnO, 3% Ag-ZnO and 5% Ag-ZnO nanostructure electrodes of ASCs at (1-5) A/g. ASCs based on 3% Ag-ZnO electrode exhibit a longer discharge time of approximately 320 seconds at a current density of 1 A/g. At the same current density, however, the 1% Ag-ZnO, 5% Ag-ZnO and pure ZnO electrodes has a discharge time of 220, 135 and 72 second respectively.

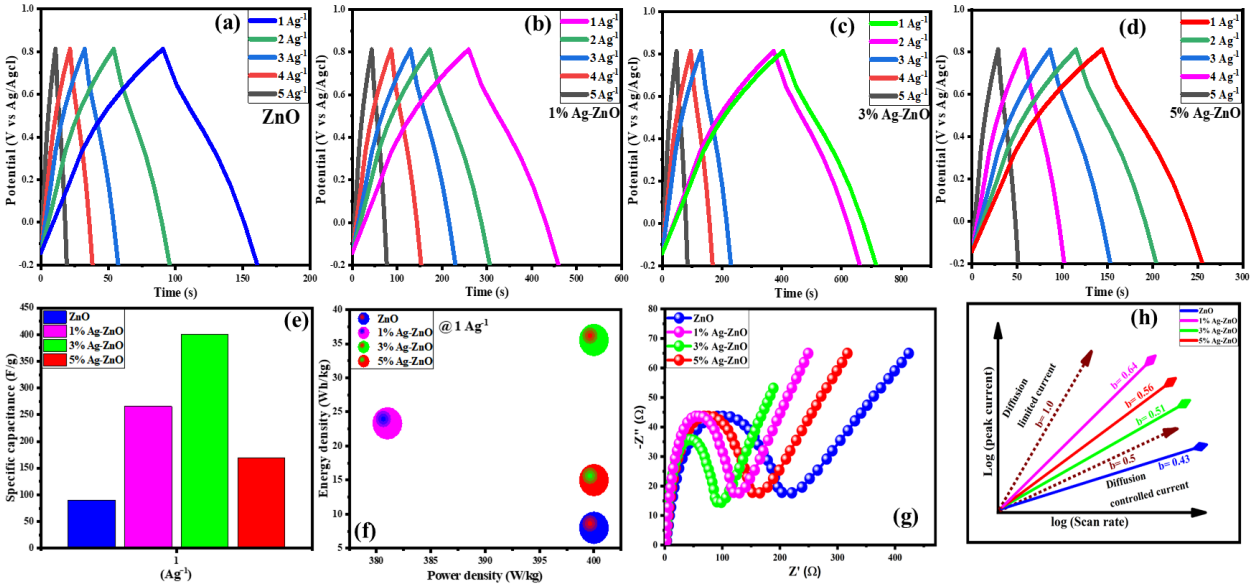


Fig.11: GCD curves of (a-d) while Cs vs current density (e) ragon plot (f) Nyquist plot (g) and calculate b values (h) of ZnO, 1% Ag-ZnO, 3% Ag-ZnO and 5% Ag-ZnO respectively.

The specific capacitance calculated from GCD, curves are 90, 265.5, 400 and, 168.75 F/g for ZnO, 1% Ag-ZnO, 3% Ag-ZnO and 5% Ag-ZnO respectively. The GCD profile of the electrodes shows battery-like activity between 0 and 0.8 V, which is the operating potential window [89]. To illustrate the performance of the ASCs, the Ragone plot, which shows the energy density (Wh/kg) against the power density (W/kg), is shown in Fig.11 (f). The calculated ASC characteristics at 1 A/g are shown in table 3, where the 3% Ag-ZnO electrode has an energy density of approximately (˜35.55 Wh/kg), which is higher than that of the 1% Ag-ZnO (˜23.33 Wh/kg), 5% Ag-ZnO (˜15 Wh/kg), and ZnO (˜8 Wh/kg). The maximum power densities reported for ZnO, 1% Ag-ZnO 3% Ag-ZnO and 5% Ag-ZnO are 1600 W/kg, 1657.14 W/kg, 1688 W/kg and 1500.98 W/kg, at 5 A/g respectively. The 1% Ag-ZnO, 3% Ag-ZnO and 5% Ag-ZnO electrodes show superior specific capacitance and energy density compare to pure ZnO indicate that Ag improve the electrical conductivity, enhance redox activity and improve surface morphology and active sites making Ag doped ZnO nanostructures as efficient and

promising electrode for energy storage applications.

Table3. Calculated C_s, energy density and power density, Charge transfer resistance and solution resistance for supercapacitor.

Electrode	Current density (A/g)	Specific capacitance (F/g)	Energy density (Wh/kg)	Power density (W/kg)	Charge transfer resistance (Rct) (Ω)	Solution resistance (Rs) (Ω)
ZnO	1	90	8	400	220	3.2
1% Ag-ZnO	1	265.5	23.33	381.81	115	2.2
3% Ag-ZnO	1	400	35.55	400	90.5	1.8
5% Ag-ZnO	1	168.75	15	400	150	2.7

Conclusion

In this work ZnO, and Ag-dopped ZnO (Ag-ZnO) nanostructures were successfully synthesized via facile hydrothermal method and systematically investigated for photocatalytic, electrocatalytic and energy storage applications. X-ray diffraction (XRD) confirmed the crystalline nature for ZnO and Ag-ZnO with no impurity phases, indicating successful incorporation of Ag in the ZnO. Scanning electron microscopy (SEM) revealed a nanowire morphology for pristine ZnO, while Ag-ZnO exhibited nanowires decorated on nanorods demonstrating significant morphological modification due to Ag doping. Energy disperse X-ray spectroscopy (EDS) verified the elemental composition and confirmed the presence of Zn, O in the ZnO, while Zn, O and Ag in the Ag-ZnO. Photocatalytic degradation studies demonstrated that Ag-ZnO exhibits superior photocatalytic performance compare to pristine ZnO, attributed to enhanced charge separation and improve light absorption. Linear sweep voltammetry (LSV) analysis revealed that 3% Ag-ZnO have over potential of 183 V and Tafel slope of 48 $mVdec^{-1}$ for hydrogen evolution reaction (HER) and overpotential of 180 V and Tafel slope of 52.43 $mVdec^{-1}$ oxygen evolution reaction (OER). Further electrochemical studied show highest specific capacitance of 388.4 F/g at 20 mVs^{-1} for 3% Ag-ZnO from Cyclic voltammetry curve (CV). Electrochemical impedance spectroscopy (EIS) showed lowest charge transfer resistance of 93 Ω, for 3% Ag-ZnO. Galvanostatic charge discharge (GCD) showed highest specific capacitance of 400 F/g at 1 A/g, energy density of 35.55 Wh/kg at 1 A/g and power density of 1688 W/kg at 5 A/g. These results highlight Ag-ZnO as a promising multifunctional material for photocatalytic, electrocatalyst and advanced energy storage applications.

References

1. Ahmad, K., et al., *Enhanced supercapacitor performance of copper-doped NiO nanostructures synthesized via hydrothermal method.* 2025: p. 113060.
2. Lemago, H.H., et al., *Enhanced photocatalysis via inverse opal structures: Synthesis and characterization of TiO2/ZnO and ZnO/TiO2 composites using plasma-enhanced ALD.* 2025. **51**(1): p. 339-352.
3. Halim, O.M.A., et al., *A review on modified ZnO for the effective degradation of methylene blue and rhodamine B.* 2025. **18**: p. 100408.
4. Roushree, R., et al., *Recent advances in ZnO-based nanocomposites for amoxicillin photocatalytic degradation and adsorption in wastewater: a review.* 2025: p. 1-38.
5. Heris, S.Z., P.B. Khaniani, and S.B.J.J.o.W.P.E. Mousavi, *Photocatalytic degradation of co-amoxiclav using hybrid TiO2/ZnO nanoparticles: Experimental and optimization.* 2025. **70**: p. 107040.

6. Muhammad, H., et al., *ZnO based photocatalysts for pesticides degradation.* 2025. **15**(58): p. 49852-49874.
7. Khan, M.G.I., et al., *Hydrothermal synthesis of CeO2/ZnO heterojunctions for effective photocatalytic degradation of organic pollutants.* 2025. **322**: p. 118630.
8. Sun, X., et al., *A photocatalyst combined of copper doped ZnO and graphdiyne (Cu/ZnO@ GDY) for photocatalytic degradation of tetracycline: Mechanism and application.* 2025. **278**: p. 123345.
9. Eswaran, P., et al., *Sunlight-driven photocatalytic degradation of methylene blue using ZnO/biochar nanocomposite derived from banana peels.* 2025. **15**(8): p. 12347-12367.
10. Mazarji, M., et al., *Synthesis, characterization, and enhanced photocatalytic dye degradation: Optimizing graphene-based ZnO-CdSe nanocomposites via response surface methodology.* 2025. **1010**: p. 177999.
11. Sumantrao, S.K., et al., *Sunlight-driven GO/ZnO nanocomposite for photocatalytic degradation of Chlorpyrifos insecticide and its biological activities.* 2025. **13**(2): p. 115437.
12. Ranjbari, A., et al., *Comparative photocatalytic degradation of cationic rhodamine B and anionic bromocresol green using reduced ZnO: A detailed kinetic modeling approach.* 2025. **371**: p. 144052.
13. Ma, B., et al., *Photocatalytic degradation of methylene blue using ZnO modified with nano-biochar derived from bacterial cellulose.* 2025. **51**(11): p. 14948-14956.
14. Kumar, S.A., et al., *Fabrication of N-doped ZnO for evaluation of photocatalytic degradation of methylene blue, methyl orange and improved supercapacitor efficiency under redox-active electrolyte.* 2025. **186**: p. 109052.
15. Jaihindh, D.P., et al., *Heterogeneous Z-scheme CuO/ZnO aerogel photocatalyst for photocatalytic degradation of organic dye.* 2025. **175**: p. 106281.
16. Padmanabhan, N.T., et al., *ZnO/Mo2TiC2 MXene nanohybrids for enhanced solar-driven photocatalytic degradation of tetracycline and organic pollutants in contaminated water.* 2025. **1**(3): p. 100042.
17. Abdulqodus, A.N., et al., *Green synthesis of ZnO nanoparticles: effect of pH on morphology and photocatalytic degradation efficiency.* 2025. **131**(9): p. 720.
18. Mahajan, M., et al., *Green synthesis of ZnO nanoparticles using Justicia adhatoda for photocatalytic degradation of malachite green and reduction of 4-nitrophenol.* 2025. **15**(4): p. 2958-2980.
19. Pan, T., et al., *The promoted Fenton degradation of norfloxacin by a S-ZnO modified MnFe2O4 with micro-acidic environment.* 2025. **506**: p. 159898.
20. Sowndharya, S., M. Nikitha, and S.J.J.o.C.P. Meenakshi, *Designing an in-situ embedment of citric acid@ HAp/ZnO as a Z-scheme heterojunction for substantial enhancement in photocatalytic degradation of malachite green under visible light.* 2025. **490**: p. 144723.
21. Asif, M., et al., *Photocatalytic degradation of methyl orange from aqueous solution using ZnO by response surface methodology.* 2025. **68**(9): p. 814-822.
22. Wilson, J., et al., *Evaluation of photocatalytic ZnO-geopolymer composites: degradation of methylene blue and α-pinene.* 2025: p. 106125.
23. Quy, B., et al., *Photocatalytic degradation performance of a chitosan/ZnO–Fe 3 O 4 nanocomposite over cationic and anionic dyes under visible-light irradiation.* 2025. **15**(3): p. 1590-1603.
24. Elahian, M., et al., *Preparation of a polyaniline-supported Ce-Ag-doped ZnO nanocomposite for efficient photocatalytic degradation of acid blue 113 dye.* 2025. **25**: p. 103824.

25. Kumaran, A.V., et al., *Sustainable production of ZnO/MgO nanocomposite for effective photocatalytic degradation of Rhodamine B and their other properties.* 2025. **313**: p. 117866.
26. Huang, P., et al., *A stable and reusable Z-scheme ZnO/Ag2CO3 photocatalyst for efficient degradation of emerging water pollutants.* 2025: p. 113663.
27. Xu, Y., et al., *Ultrahigh-performance NiWO4 nanoparticles anchored ZnO nanoflakes as a potential electrode for energy storage applications.* 2025. **381**: p. 133395.
28. Shah, M.Z.U., et al., *Enhanced energy storage with TiO2/NiO/ZnO core-shell heterostructures in hybrid battery-supercapacitor applications.* 2025. **1013**: p. 178548.
29. Zhou, R. and K.H.J.J.o.E.S. Lam, *ZnO@ Ni symmetric supercapacitors in application of sustainable energy storage.* 2025. **107**: p. 114991.
30. Lakshmipriya, M., et al., *Influence of the codopants and calcination temperature in enhancing the electrochemical and dielectric properties of ZnO nanoparticles for energy storage applications.* 2025. **114**: p. 115868.
31. Qin, X., et al., *Particle size effect of nano-ZnO fillers on the dielectric and energy storage properties of PI/ZnO composite films.* 2025. **1013**: p. 178624.
32. Agrahari, D.S., et al., *Fabrication of Ag doped CuO/ZnO nanocomposite for high-performance asymmetric supercapacitor device.* 2025: p. 100100.
33. Sasikumar, K., et al., *Influence of natural carbon template on Ag-ZnO nanocomposites for enhanced supercapacitor, photocatalytic hydrogen production and antifungal activity.* 2025. **193**: p. 109523.
34. Nethaji, P., P.S.J.C.E.R. Kumar, and Design, *V-Ag doped ZnO nanorod as high-performance electrode material for supercapacitors with enhanced specific capacitance and cycling stability.* 2022. **178**: p. 356-368.
35. Mourya, A.K., et al., *ZnO/Ag2ZrO3 nanocomposites: A tailored nanostructure for enhanced supercapacitor, photocatalytic & antimicrobial applications.* 2024. **1004**: p. 175792.
36. Purty, B., et al. *Remarkable enhancement in electrochemical capacitance value of Ag-ZnO/PANI composite for supercapacitor application.* in *AIP Conference Proceedings*. 2019. AIP Publishing LLC.
37. Kumar, A., et al., *Facile synthesis of silver-ZnO composite for enhanced electrochemical performance in supercapacitor applications.* 2025. **100**(12): p. 125901.
38. ur Rehman, A., et al., *Impact of ZnO on structural and electrochemical properties of silver spinel ferrites for asymmetric supercapacitors.* 2023. **931**: p. 117206.
39. Sasirekha, C., S. Arumugam, and G.J.A.S.S. Muralidharan, *Green synthesis of ZnO/carbon (ZnO/C) as an electrode material for symmetric supercapacitor devices.* 2018. **449**: p. 521-527.
40. Solís-Cortés, D., et al., *A solid-state integrated photo-supercapacitor based on ZnO nanorod arrays decorated with Ag 2 S quantum dots as the photoanode and a PEDOT charge storage counter-electrode.* 2020. **10**(10): p. 5712-5721.
43. Bhirud, A., et al., *In situ preparation of N–ZnO/graphene nanocomposites: excellent candidate as a photocatalyst for enhanced solar hydrogen generation and high performance supercapacitor electrode.* 2015. **3**(33): p. 17050-17063.
44. Abdelhamid, H.N., S.A. Al Kiey, and W.J.A.O.C. Sharmoukh, *A high-performance hybrid supercapacitor electrode based on ZnO/nitrogen-doped carbon nanohybrid.* 2022. **36**(1): p. e6486.
45. Samuel, E., et al., *ZnO/MnO x nanoflowers for high-performance supercapacitor electrodes.* 2020. **8**(9): p. 3697-3708.

46. Shaheen, I., et al., *Facile ZnO-based nanomaterial and its fabrication as a supercapacitor electrode: synthesis, characterization and electrochemical studies.* 2021. **11**(38): p. 23374-23384.
47. Ali, A., et al., *Mo-doped ZnO nanoflakes on Ni-foam for asymmetric supercapacitor applications.* 2019. **9**(47): p. 27432-27438.
48. BaQais, A., et al., *Probe-sonicated synthesis of CuO–ZnO hybrid nanocomposite for photocatalytic and supercapacitor applications.* 2023. **11**(9): p. 370.
49. He, X., et al., *Morphology engineering of ZnO nanostructures for high performance supercapacitors: enhanced electrochemistry of ZnO nanocones compared to ZnO nanowires.* 2017. **28**(24): p. 245402.
50. Luo, Q., et al., *Synthesis of ZnO tetrapods for high-performance supercapacitor applications.* 2017. **198**: p. 192-195.
51. Gao, M., et al., *Porous ZnO-coated Co3O4 nanorod as a high-energy-density supercapacitor material.* 2018. **10**(27): p. 23163-23173.
52. Jayachandiran, J., et al., *Synthesis and electrochemical studies of rGO/ZnO nanocomposite for supercapacitor application.* 2018. **28**(5): p. 2046-2055.
53. Wang, L., et al., *A novel core-shell structured hybrid composed of zinc homobenzotrizoate and silver borotungstate with supercapacitor and photocatalytic dye degradation performance.* 2022. **46**: p. 103873.
54. Altaf, C.T., et al., *Photo-supercapacitors based on nanoscaled ZnO.* 2022. **12**(1): p. 11487.
55. Aravinda, L., et al., *ZnO/carbon nanotube nanocomposite for high energy density supercapacitors.* 2013. **95**: p. 119-124.
56. Zahra, T., et al., *Boosting the energy-storing performance of hydrothermally synthesized ZnO by MnTe for supercapacitor applications.* 2024. **35**(16): p. 1086.
57. Ambujam, K., et al., *Studies on electrochemical properties of ZnO/CuMn2O4 NCs as electrode material for supercapacitor application.* 2024. **35**(8): p. 578.
58. Selvakumar, M., et al., *Nano ZnO-activated carbon composite electrodes for supercapacitors.* 2010. **405**(9): p. 2286-2289.
59. Büyükkürkçü, H., et al., *Investigation of the performance and properties of ZnO/GO double-layer supercapacitor.* 2024. **191**: p. 111984.
60. Zhu, C., et al., *ZnO@ MOF@ PANI core-shell nanoarrays on carbon cloth for high-performance supercapacitor electrodes.* 2019. **35**: p. 124-131.
61. Haldorai, Y., W. Voit, and J.-J.J.E.A. Shim, *Nano ZnO@ reduced graphene oxide composite for high performance supercapacitor: Green synthesis in supercritical fluid.* 2014. **120**: p. 65-72.
62. Khan, A.J., et al., *Synthesis of heterostructured ZnO-CeO2 nanocomposite for supercapacitor applications.* 2024. **159**: p. 111794.
63. Lee, K.S., et al., *Synthesis of ZnO/activated carbon with high surface area for supercapacitor electrodes.* 2018. **555**: p. 482-490.
64. Kim, S.-I., et al., *Facile route to an efficient NiO supercapacitor with a three-dimensional nanonetwork morphology.* 2013. **5**(5): p. 1596-1603.
65. Dar, F.I., K.R. Moonoosawmy, and M.J.N.r.l. Es-Souni, *Morphology and property control of NiO nanostructures for supercapacitor applications.* 2013. **8**(1): p. 363.
66. Dhas, S.D., et al., *Synthesis of NiO nanoparticles for supercapacitor application as an efficient electrode material.* 2020. **181**: p. 109646.
67. Cai, G., et al., *Electrochromo-supercapacitor based on direct growth of NiO nanoparticles.* 2015. **12**: p. 258-267.
68. Vijayakumar, S., et al., *Supercapacitor studies on NiO nanoflakes synthesized through a microwave route.* 2013. **5**(6): p. 2188-2196.

International Journal of Advanced Research

69. Badreldin, A., A. Abdel-Wahab, and P.B.J.A.A.E.M. Balbuena, *Local surface modulation activates metal oxide electrocatalyst for hydrogen evolution: synthesis, characterization, and DFT study of novel black ZnO*. 2020. **3**(11): p. 10590-10599.
70. Hanan, A., et al., *Co3O4 derived ZnO: An effective electrocatalyst for oxygen evolution reaction in alkaline media*. 2025. **104**: p. 407-415.
71. Nie, M., et al., *Study on electrocatalytic property of ZnO and Ag/ZnO*. 2020. **271**: p. 127785.
72. Shakil, M.R., et al., *Single-doped and multidoped transition-metal (Mn, Fe, Co, and Ni) ZnO and their electrocatalytic activities for oxygen reduction reaction*. 2018. **57**(16): p. 9977-9987.
73. Kanase, R.S., et al., *Highly selective and durable CO production via effective morphology and surface engineering of ZnO electrocatalysts*. 2022. **5**(11): p. 13913-13927.
74. Mugheri, A.Q., A.A. Otho, and A.A.J.J.o.E.C. Mugheri, *Hierarchical fibrous bimetallic electrocatalyst based on ZnO-MoS2 composite nanostructures as high performance for hydrogen evolution reaction*. 2021. **883**: p. 115061.
75. Alahmari, S.D., et al., *Hydrothermal synthesis of ZnO@ MoTe2 nanocomposite as excellent electrocatalyst for hydrogen evolution reaction (HER)*. 2024. **358**: p. 130275.
76. Wu, H.-C., et al., *Enhanced Zn/ZnO Heterointerfaces via Pulsed-Potential Electrochemical Reconstruction for Highly Selective CO2 Reduction*. 2025. **17**(41): p. 56991-57001.
77. Ding, L., et al., *Synchronous generation of green oxidants H 2 O 2 and O 3 by using a heterojunction bifunctional ZnO/ZnS@ C electrocatalyst*. 2023. **11**(7): p. 3454-3463.
78. Saini, B., et al., *Role of ZnO in ZnO nanoflake/Ti3C2 MXene composites in photocatalytic and electrocatalytic hydrogen evolution*. 2022. **5**(7): p. 9319-9333.
79. Al-Bataineh, Q.M., et al., *Unveiling the role of UV-induced defects in Al-doped ZnO for enhanced electrocatalytic water splitting*. 2026: p. 165821.
80. Zhou, Y., et al., *Oxygen reduction reaction electrocatalysis inducing Fenton-like processes with enhanced electrocatalytic performance based on mesoporous ZnO/CuO cathodes: Treatment of organic wastewater and catalytic principle*. 2020. **259**: p. 127463.
81. Choo, T.-F., et al., *Electrocatalytic and photocatalytic activities of hierarchically structured zinc oxide nanoparticles derived from cellulose paper-precipitated hydrozincite*. 2023. **49**(23): p. 39180-39188.
82. Wang, H., et al., *Fabrication of ZnO nanosheets self-assembled by nanoparticles for accelerated electrocatalytic reduction of CO2 to CO*. 2023. **333**: p. 126431.
83. Kwak, I., et al., *IrO2–ZnO hybrid nanoparticles as highly efficient trifunctional electrocatalysts*. 2017. **121**(27): p. 14899-14906.
84. Fareed, I., et al., *N–ZnO/g-C3N4 nanoflowers for enhanced photocatalytic and electrocatalytic performances*. 2024. **164**: p. 116053.
85. Ingavale, S., et al., *Starbon with Zn-N and Zn-O active sites: An efficient electrocatalyst for oxygen reduction reaction in energy conversion devices*. 2021. **370**: p. 55-65.
86. Pataniya, P.M., D. Late, and C.J.A.A.E.M. Sumesh, *Photosensitive WS2/ZnO nano-heterostructure-based electrocatalysts for hydrogen evolution reaction*. 2021. **4**(1): p. 755-762.
87. Yadav, P., et al., *Zinc oxide-based nanomaterials as efficient photocatalysts and electrocatalysts*. 2025. **31**(9): p. 8875-8901.

88. Junaid, A., et al., *Developing Ag3VO4@ ZnO electrode material for efficient oxygen evolution reaction showcasing its potential for sustainable energy applications*. 2025. **379**: p. 133029.

89. Alhashmialameer, D., et al., *Improved catalytic performance of (Fe, Cr)-ZnO/g-C3N4 nanocomposite towards electrocatalytic water splitting for clean energy*. 2025. **160**: p. 107823.

International Journal of Advanced Research